Journal of Advanced Research 47 (2023) 209–223

Contents lists available at ScienceDirect

Journal of Advanced Research

journal homepage: www.elsevier.com/locate/jare

Original Article

# Medical gas plasma augments bladder cancer cell toxicity in preclinical models and patient-derived tumor tissues

Nadine Gelbrich [a,b], Lea Miebach [b,c], Julia Berner [b,d], Eric Freund [b,c], Fariba Saadati [b,e], Anke Schmidt [b], Matthias Stope [f], Uwe Zimmermann [a], Martin Burchardt [a], Sander Bekeschus [b,*]

[a] Clinic and Policlinic for Urology, Greifswald University Medical Center, Ferdinand-Sauerbruch-Str., 17475 Greifswald, Germany
[b] ZIK plasmatis, Leibniz Institute for Plasma Science and Technology (INP), Felix-Hausdorff-Str. 2, 17489 Greifswald, Germany
[c] Clinic and Policlinic for General, Visceral, Thoracic, and Vascular Surgery, Greifswald University Medical Center, Ferdinand-Sauerbruch-Str., 17475 Greifswald, Germany
[d] Clinic and Policlinic for Oral, Maxillofacial, and Plastic Surgery, Greifswald University Medical Center, Ferdinand-Sauerbruch-Str., 17475 Greifswald, Germany
[e] Clinic and Policlinic of Dermatology and Venerology, Rostock University Medical Center, Stempelstr. 13, 18057 Rostock, Germany
[f] Department of Gynecology and Gynecological Oncology, University Hospital Bonn, 53127 Bonn, Germany

## HIGHLIGHTS

- Gas plasma is a novel ROS-generating tool that can be used in oncology.
- Bladder cancer cells in 2D, 3D, semi-in vivo (in ovo), and in patient-derived samples were employed.
- Tumor cells in all models were inactivated following gas plasma treatment.
- The reactive oxygen species production was assessed in detail.
- Several mechanistic targets identified in cancer patient tissues, such as FGFR3, using whole transcriptome analysis.

## GRAPHICAL ABSTRACT

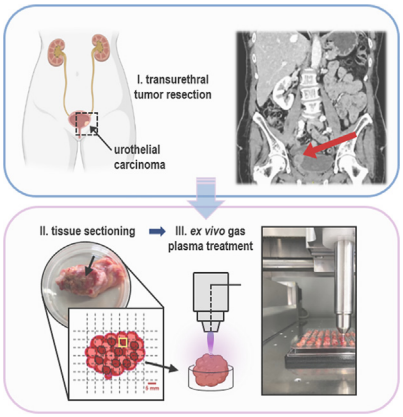


## ARTICLE INFO

*Article history:*
Received 30 November 2021
Revised 8 June 2022
Accepted 29 July 2022
Available online 3 August 2022

*Keywords:*
Apoptosis
Cancer
Cold physical plasma
Oncology
Reactive oxygen and nitrogen species
Urology

## ABSTRACT

*Introduction:* Medical gas plasma therapy has been successfully applied to several types of cancer in preclinical models. First palliative tumor patients suffering from advanced head and neck cancer benefited from this novel therapeutic modality. The gas plasma-induced biological effects of reactive oxygen and nitrogen species (ROS/RNS) generated in the plasma gas phase result in oxidation-induced lethal damage to tumor cells.
*Objectives:* This study aimed to verify these anti-tumor effects of gas plasma exposure on urinary bladder cancer.
*Methods:* 2D cell culture models, 3D tumor spheroids, 3D vascularized tumors grown on the chicken chorion-allantois-membrane (CAM) *in ovo*, and patient-derived primary cancer tissue gas plasma-treated *ex vivo* were used.
*Results:* Gas plasma treatment led to oxidation, growth retardation, motility inhibition, and cell death in 2D and 3D tumor models. A marked decline in tumor growth was also observed in the tumors grown *in ovo*. In addition, results of gas plasma treatment on primary urothelial carcinoma tissues *ex vivo* highlighted the selective tumor-toxic effects as non-malignant tissue exposed to gas plasma was less affected.

Peer review under responsibility of Cairo University.
* Corresponding author.
*E-mail address:* sander.bekeschus@inp-greifswald.de (S. Bekeschus).

https://doi.org/10.1016/j.jare.2022.07.012

Whole-transcriptome gene expression analysis revealed downregulation of tumor-promoting fibroblast growth factor receptor 3 (FGFR3) accompanied by upregulation of apoptosis-inducing factor 2 (AIFm2), which plays a central role in caspase-independent cell death signaling.
*Conclusion:* Gas plasma treatment induced cytotoxicity in patient-derived cancer tissue and slowed tumor growth in an organoid model of urinary bladder carcinoma, along with less severe effects in non-malignant tissues. Studies on the potential clinical benefits of this local and safe ROS therapy are awaited.


## Introduction

With about 550,000 annual new cases worldwide, carcinomas of the urinary bladder rank among the most frequently diagnosed malignancies and represent the second most common urogenital tumor after prostate cancer [1,2]. With a median age of onset above 70 and an anticipated increase in life expectancy worldwide, case numbers are most likely to rise in the future [3]. The variable appearance and strong genetic heterogeneity (4th most frequent mutation rate) of urinary bladder carcinoma [4] require differentiated diagnostics and stage-adapted, multimodal therapies, including surgical interventions, systemic cisplatin-based chemotherapy, and checkpoint-based immunotherapies [5–7]. Nevertheless, 30 % of patients develop highly aggressive, muscle-invasive tumor growth with a high risk of mortality and metastasis [8–10], resulting in a poor 5-year survival rate of only 50 % [11]. Additionally, severe side effects caused by some treatment modalities, such as platinum-based chemotherapeutic drugs, highlight the urgent need for novel therapeutic options in bladder cancer [12,13].

In the past years, medical gas plasma technology has become of emerging interest in oncological research [14]. Such plasmas are ignited by partial gaseous ionization and feature a versatile mix of reactive oxygen and nitrogen species (ROS/RNS) capable of eliciting oxidative distress in tumor cells when applied at supraphysiological levels [15]. Notably, technological leap innovations allowed the generation and application of such gas plasmas at body temperature, facilitating the exposure of diseased tissue without thermal harm or necrotizing effects [16]. Following gas plasma-mediated oxidative distress [17], biological signaling pathways are activated that mediate diverse beneficial anti-tumor effects, including reduced tumor cell proliferation and the induction of apoptotic or immunogenic cell death [18,19].

Previously, some attention was given to prostate and gynecological cancer cells exposed to gas plasma *in vitro* [20,21]. The present study aimed to investigate medical gas plasma technology for its tumor-toxic potential in treating urinary bladder cancer. Following ROS/RNS characterization of the gas plasma treatment setup, four human bladder cancer cell lines were investigated for oxidation, metabolic activity, cytotoxicity, motility, and mitochondrial content. In addition, key results on gas plasma-mediated cytotoxicity were re-iterated in 3D tumor spheroids grown *in vitro* and 3D vascularized tumors grown on the chorioallantois-membrane of chicken embryos (*in ovo*). Finally, an urothelial carcinoma patient cohort was established to test primary human tumor material following gas plasma exposure *ex vivo*. Besides cytotoxicity, global gene expression profiling (transcriptomics) served to identify molecular signatures associated with the treatment. This is the first study to comprehensively investigate the effects of a certified medical device argon plasma jet across several bladder cancer models from *in vitro* investigations to patient-derived tumor tissue to demonstrate the promising nature of medical gas plasma therapy in future urological oncology.

## Materials and methods

### *Gas plasma jet and treatment*

Gas plasma treatment was performed using the atmospheric pressure plasma jet kINPen MED (neoplas tools, Greifswald, Germany) as outlined before [22]. The jet is accredited as a medical device in Europe, and its physical and chemical properties have been extensively described [23]. The jet was operated with three standard liters of argon (99.999 % purity; Air Liquide, Germany) per minute, adjusted by a high-precision mass flow controller (MKS, Germany). Standardized treatment heights and procedures were achieved using a computer-controlled and motorized xyz table (CNC, Germany) that hoovered the kINPen over the center of each well or tissue biopsy for a preconfigured time length.

### *Gas phase and liquid phase ROS/RNS analysis*

In order to investigate reactive species (ROS/RNS) present in the plasma gas phase, optical emission spectroscopy (OES) was performed as described before [24]. Briefly, the gas plasma jet was positioned in front of a UV-sensitive optical emission spectrometer (AvaSpec-2048-USB2; Avantes, Germany) with a spectral resolution of 0.7 nm. Emission spectra between 200 and 900 nm were recorded end-on at the center of the plasma effluent. For quantification of ROS/RNS deposition in liquids, 500 µl of 0.9 % sodium chloride solution (NaCl; Pan Biotech, Germany) were exposed to gas plasma for 15 s, 30 s, 45 s, 60 s, or 90 s in a 24-well plate (Greiner Bio-One, Germany) in the presence or absence of urothelial cancer cells. Liquid analysis was performed immediately (NaCl only) and 1 h after treatment (NaCl containing cells). Changes in pH were measured using a pH meter (Mettler-Toledo, Germany). Quantification of hydrogen peroxide ($H_2O_2$) in gas plasma-oxidized liquids was performed using the *Amplex Ultra Red* Assay (Thermo Fisher, Germany) according to the manufacturer's instructions. Fluorescence was determined using a multimode plate reader (F200; Tecan, Switzerland) at $\lambda_{ex}$ 535 nm and $\lambda_{em}$ 590 nm. The concentration of nitrite ($NO_2^-$) and nitrate ($NO_3^-$) was determined using the *Griess* assay (Cayman Chemical, Germany) following the supplier's instructions. Absorbance was measured at 540 nm with a multiplate reader (M200; Tecan, Switzerland). In all assays, absolute concentrations were calculated against a standard curve. The carrier gas argon itself served as a mock control in all experimental conditions.

### *Cell culture*

The human urothelial carcinoma cell lines T24, RT-112, CLS-439 (abbreviated here as CLS; CLS Cell lines Service, Germany), and SCaBER (squamous differentiation) (all others: ATCC, USA) were cultivated in Roswell Park Memorial Institute (RPMI) 1640 medium (Pan Biotech, Germany) supplemented with 10 % fetal bovine serum, 1 % penicillin/streptomycin, and 1 % glutamine (all Corning, Germany). Cells were kept under standard culture conditions at

37 °C, 5 % $CO_2$, and 95 % humidity in a cell culture incubator (Binder, Germany). Twenty-four hours before experiments, $5x10^4$ cells in 500 µl fully-supplemented medium were seeded in 24-well plates (Greiner Bio-One, Germany). After gas plasma exposure, evaporated liquid was compensated for by adding predetermined amounts of double-distilled $H_2O$.

*Intracellular ROS/RNS analysis*

Cells were stained with 2 µM 2′,7′-dichlorodihydrofluorescein diacetate (DCF-DA; Thermo Fisher, Germany) for 30 min at 37 °C. After washing, cells were exposed to gas plasma for 60 s in PBS. DCF fluorescence intensity was evaluated using fluorescence microscopy (Operetta CLS; PerkinElmer, Germany) immediately, 6 h, and 12 h after treatment. Images were acquired in brightfield and fluorescence channels ($\lambda_{ex}$ 475 nm and $\lambda_{em}$ 525 nm for DCF) using a 20x air objective (NA = 0.4). Image acquisition parameters and unsupervised algorithm-based image analysis were performed using *Harmony 4.9* software (PerkinElmer, Germany).

*Metabolic activity*

The metabolic activity of cells was assessed using 100 µM 7-hydroxy-3H-phenoxazin-3-on-10-oxid (resazurin; Alfa Aesar, USA) 21 h after gas plasma treatment and after 3 h of incubation under standard culture conditions. Viable cells metabolize non-fluorescent resazurin to fluorescent resorufin in a $NADPH/H^+$-dependent reaction measured at $\lambda_{ex}$ 535 nm and $\lambda_{em}$ 590 nm using a multimode plate reader (F200; Tecan, Switzerland). Wells containing complete cell culture medium and resazurin served as background controls, and results were normalized to mock gas treatments.

*Viability and motility*

Viability was evaluated 24 h after gas plasma treatment using flow cytometry. Here, cells were stained with 0.5 µM *CellEvent Caspase 3/7 detection* reagent (Thermo Fisher, Germany) for 30 min at 37 °C to identify apoptotic cells, and samples were acquired using flow cytometry (CytoFLEX S; Beckman-Coulter, Germany). In addition, terminal cell death was followed dynamically using kinetic fluorescence imaging. For this, cells were stained with 1 µM 4′,6-Diamidin-2-phenylindol (DAPI; Sigma Aldrich, Germany) to stain nuclei of terminally dead cells and 0.1 µM *MitoTracker Deep Red* (MTR; Thermo Fisher, Germany) to stain mitochondria. Mitochondrial staining with MTR is dependent on mitochondrial membrane potential and can be used as an indicator for mitochondrial stress levels and induction of apoptosis. Images were acquired in brightfield and respective fluorescence channels ($\lambda_{ex}$ 365 nm and $\lambda_{em}$ 465 nm for DAPI; $\lambda_{ex}$ 630 nm and $\lambda_{em}$ 680 nm for MTR) using a 20x air objective (NA = 0.4) in nine fields of view per well, each being 422.5 $\mu m^2$ (total area: 3.8 $mm^2$), and triplicate wells were measured per condition in each of three independent experiments. Image acquisition parameters and unsupervised algorithm-based image analysis were performed using *Harmony 4.9* software (PerkinElmer, Germany).

*Doubling-time assessment*

In order to assess the cellular division rate, $0.5x10^3$ cells in 100 µl of fully supplemented cell culture medium were seeded per well of a 96-well flat-bottom plate. Cells were fixed every 24 h using fixation buffer (BioLegend, The Netherlands) until 96 h after initial cell seeding. After permeabilization (Permeabilization Wash Buffer; BioLegend, The Netherlands), cells were stained with 10 µM of DAPI. Total cell counts were evaluated using high content imaging (Operetta CLS). Images were acquired using a 10x Air objective (NA = 0.3) in twelve fields of view per well in each of three experiments per condition. Image acquisition parameters and algorithm-based analysis were performed using Harmony 4.9 software (PerkinElmer, Germany).

*Colony formation assay*

$1x10^3$ cells in 0.35 % soft agar were seeded in each well of a 96-well flat-bottom plate. Fifty microliters of fully supplemented cell culture medium were added to each well on top of the soft agar to ensure sufficient nutrient supply. Cells were incubated for 3 weeks at standard culture conditions until colony formation was assessed using high content imaging and Harmony Software analysis. Brightfield images were acquired using a 5x Air objective (NA = 0.16).

*3D tumor spheroids*

Three-dimensional (3D) urothelial carcinoma spheroids were prepared by seeding $2x10^4$ cells per well in a 96-well ultra-low attachment plate (Thermo Fisher, Germany) and following centrifugation at 1000xg for 10 min. Cells were incubated for two days to allow spheroid formation. After 48 h, spheroids were exposed to gas plasma for 30 s, 60 s, or 90 s or argon gas only as mock control. Immediately after gas plasma treatment, spheroids were stained with 0.1 µM Sytox Green (SG; Thermo Fisher, Germany) to label terminally dead cells. Evaluation of gas plasma-mediated tumor toxicity was done using fluorescence imaging 0 h, 24 h, and 48 h after treatment. Images were acquired in brightfield and fluorescence channels ($\lambda_{ex}$ 475 nm and $\lambda_{em}$ 525 nm for SG) with a 5x air objective (NA = 0.16) and ten z-stacks per well and spheroid. The brightfield signal was inverted for image analysis, and an intensity cut-off was defined to distinguish the spheroid region from the background. In this area, the mean fluorescence intensity (MFI) of SG was quantified. Image acquisition parameters and unsupervised algorithm-based image analysis were performed using *Harmony 4.9* software (PerkinElmer, Germany).

*3D in ovo tumor model*

Fully vascularized three-dimensional tumors were grown on the hen's egg test of the chorioallantois membrane (HET-CAM) in chicken embryos as described previously [25]. Briefly, pathogen-free eggs (Valo BioMedia, Germany) were kept in a breeding incubator at 37 °C and 60 % humidity. On the prepared CAM on day 7, $1x10^6$ urothelial cancer cells in 15 µl matrigel (Corning, Germany) were seeded in a silicone ring and incubated for additional 3 days to allow tumor growth. Gas plasma treatment was performed on day 10. Treatment time per egg was 3 min. Finally, on day 14, tumor growth was assessed *ex vivo* by weighing the tumors after careful excision.

*Patient-derived urothelial carcinoma and non-malignant tissue samples*

Primary urothelial carcinoma tissue of the renal pelvis and urinary bladder was obtained from patients undergoing nephrectomy or cystectomy in the Clinic and Polyclinic for Urology Greifswald under the approval of the local ethics committee (approval number: BB 144/19a) and patients' informed consent. Additionally, healthy urothelial tissue was isolated from each patient. Immediately after isolation, the tissue was stored on ice in HEPES-buffered Krebs-Ringer solution (Thermo Fisher, Germany) until further processing to reduce tissue autolysis. For gas plasma treat-

ment, excised tumor tissue was punch-biopsied into 5 mm pieces and transferred to 96-well plates (Greiner Bio-One, Germany). Exposure times were 60 s, and argon gas served as mock control. After treatment, samples were incubated in Hank's Balanced Salt Solution (HBSS; Corning, Germany) at 37 °C, 5 % $CO_2$, and 95 % humidity for 6 h. This was followed by cryopreservation in cryo-embedding medium (Tissue-Tek OCT; Sakura Finetek, Japan) for subsequent tissue staining or dry freezing for gene expression analysis. Tissue sections (7 µm) were prepared using a cryotome (Cryostat CM1950; Leica, Germany).

### *TUNEL staining*

Labeling apoptotic cells in gas plasma-treated non-malignant and malignant tissue samples was performed using terminal deoxynucleotidyl transferase dUTP nick end labeling (TUNEL) technology (In Situ Cell Detection Kit, Fluorescein; Sigma-Aldrich, Germany) according to the supplier's instructions. Tissues were fixed in 5 % paraformaldehyde (PFA) followed by permeabilization in 0.1 % Triton X-100. Nuclei were counterstained using DAPI. Images of TUNEL-stained tissue sections were acquired using appropriate fluorescence channels ($\lambda_{ex}$ 365 nm and $\lambda_{em}$ 465 nm for DAPI; $\lambda_{ex}$ 475 nm and $\lambda_{em}$ 525 nm for TUNEL) using a pre-scanning procedure (1.25 X, NA = 0.03) of the entire microscopy slide followed by tissue imaging using 10x air objective (NA = 0.3) and a high content imaging device (Operetta CLS). Image acquisition parameters and analysis were performed using *Harmony 4.9* software (PerkinElmer, Germany). Briefly, all DAPI + objects (nuclei) within a reasonable area range (30–60 µm2) were segmented within several boarder-positioned fields of view per section. The percentage of $TUNEL^+$ objects in this population was assessed using the same quantitative image building-block algorithm across all samples investigated.

## RNA isolation and gene expression profiling

RNA was isolated from cryopreserved tissues using an RNA isolation kit (Bio & Sell, Germany) according to the manufacturer's protocol. Briefly, cryopreserved tissue was carefully thawed and transferred to a garnet matrix tube containing lysis buffer. After preparation of RNA lysates using a high-speed homogenizer (MP FastPrep-24 5G; MP Biomedicals, Germany), the RNA concentration of each sample was determined (NanoDrop 2000C; Thermo Fisher, Germany). According to the manufacturer's protocol, subsequent gene expression analysis was performed using a one-color microarray kit (low-input quick labeling kit, Agilent Technologies, Germany). Here, 200 ng RNA was prepared for complementary DNA (cDNA) synthesis and amplification. Complementary cRNA was generated, amplified, and labeled with the fluorescent dye cyanine-3, followed by cRNA purification. Finally, 600 ng labeled cRNA was used for microarray hybridization at 65 °C for 17 h. After several washing steps, microarray slides were scanned immediately using a 61 × 21.6 mm scan area at a 20bit and 3 µm resolution and evaluated with the Agilent Feature Extraction Software 10.7.3. Data analysis was performed using GeneSpring software (Agilent, Germany) and STRING database networks.

### *Statistical analysis*

Statistical analysis and graphing were performed using Prism 9.2 (GraphPad Software, USA) and *t*-test or one-way or two way analysis of variances (anova) as per figure legends. Levels of significance were as follows: p = 0.05 (*), p = 0.01 (**), p = 0.001 (***), ns = non significant. The number of independent experiments (n) is indicated in the figure legends for all data.

## Results

### *Gas plasmas generated ROS/RNS oxidizing human bladder cancer cells*

Medical gas plasmas comprise various short-lived reactive oxygen (ROS) and nitrogen (RNS) species that react to a few long-lived secondary species when introduced into liquids. Those species are capable of eliciting oxidative distress in tumor cells and can thereby mediate pronounced anti-tumor effects. In order to characterize the ROS/RNS chemistry originating from the kINPen plasma, optical emission spectroscopy (OES) and quantification of species deposition in gas plasma-oxidized liquids were performed (Fig. 1**a**). Emission spectra were recorded between 200 and 900 nm and normalized to the maximum peak at 763 nm. The spectral line at 309 nm indicated the presence of highly reactive hydroxyl radicals (·OH), whereas peaks detected between 330 and 430 nm corresponded to excited molecular nitrogen ($N_2$) species from the second positive system of $N_2$. Most spectral lines above 690 nm emanated from excited argon (Ar) molecules (Fig. 1**b**).

Since target cells in *in vitro* experiments are surrounded by bulk liquids, such as cell culture media, gas plasma-mediated effects are mainly attributed to secondary-derived ROS generated in the plasma-liquid interphase. To this end, 0.9 % sodium chloride (NaCl) was exposed to kINPen plasma for 15 s, 30 s, 45 s, 60 s, or 90 s in the presence or absence of tumor cells. Species quantification was performed immediately (NaCl only) and 60 min after gas plasma treatment (NaCl containing cells). With increasing treatment times, a decline in pH was observed (Fig. 1**c**) as the NaCl is not buffered.

Quantification of hydrogen peroxide ($H_2O_2$), which is thought to be a central mediator of gas plasma-derived biological effects *in vitro* in the presence of excessive amounts of liquids, revealed a linear increase with prolonged treatment times. After 60 min, a decline in $H_2O_2$ could be observed, which was more pronounced in the presence of cancer cells (Fig. 1**d**). Concerning secondary RNS, higher nitrite ($NO_2^-$; Fig. 1**e**) but not nitrate ($NO_3^-$; Fig. 1**f**) concentrations could be detected immediately after gas plasma treatment. Again, the concentration of $NO_2^-$ was reduced 60 min after gas plasma treatment, independent of the presence or absence of cells. For $NO_3^-$, an oxidized product of $NO_2^-$, an increase in concentration could be observed 60 min after initial treatment, which was even more pronounced in the presence of cells. Hence, gas plasma generated ROS in the plasma gas phase, which subsequently immersed into liquids to form secondary ROS/RNS·$H_2O_2$ was consumed by or reacted with the cells over time, and the latter promoted the generation of nitrate. To confirm gas plasma-derived ROS entering tumor cells, intracellular ROS were measured using quantitative microscopy of the fluorescent redox indicator DCF (dichlorofluorescein; relative fluorescence units) immediately, 6 h, and 12 h after gas plasma treatment exposure (Fig. 1**g**). Intracellular ROS increased until 6 h after gas plasma treatment and reached the baseline again after 24 h (Fig. 1**h**).

### *Cytotoxicity in gas plasma-treated 2D bladder cancer cells*

Excessive ROS/RNS exposure can elicit oxidative distress (Fig. 2**a**), which can affect metabolic activity as indicated by a shift from blue to pink color in the resazurin-resorufin-assay (Fig. 2**b**). Twenty-four hours after gas plasma exposure, a treatment time-dependent reduction in metabolic activity was observed (Fig. 2**c**). Interestingly, the sensitivity to gas plasma exposure differed considerably between the cell types investigated, as indicated by the calculated $IC_{50}$ values. RT-112 cells and CLS showed the highest resistance against gas plasma-induced decline in metabolic activity. To investigate whether this decrease was a consequence of

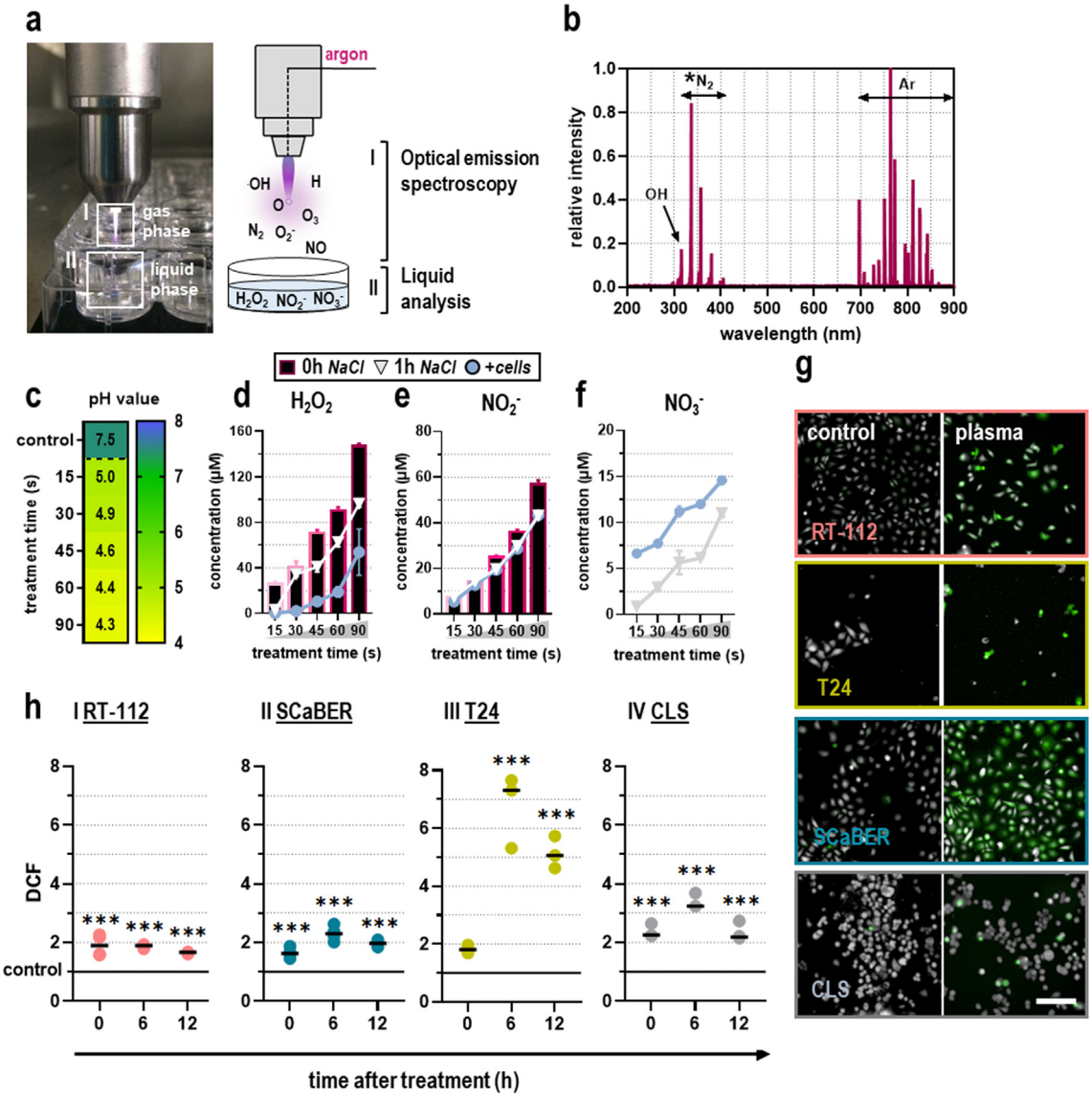


**Fig. 1. ROS/RNS profile of kINPen plasma and cellular oxidation.** (**a**) Schematic overview of ROS/RNS characterization in plasma gas and liquid phase. (**b**) Optical emission spectroscopy (OES) profile of the kINPen plasma jet indicating the presence of hydroxyl radicals (·OH), molecular nitrogen ($N_2$) as part of the second positive system of nitrogen, and excited argon (Ar) peaks (n = 10). (**c**) pH in gas plasma-oxidized NaCl (n = 3). (**d-f**) Quantification of hydrogen peroxide ($H_2O_2$; **d**), nitrite ($NO_2^-$; **e**), and nitrate ($NO_3^-$; **f**) in gas plasma-oxidized liquids immediately (bars) and 1 h after gas plasma treatment in the presence (circle) or absence (triangle) of cancer cells (n = 3); bar graphs show mean ± standard error of the mean (SEM). (**g**) Representative images of intracellular ROS evaluated via DCF fluorescence. (**h**) Quantitative image analysis of DCF fluorescence intensities immediately, 6 h, and 12 h after gas plasma treatment in malignant (**I**) RT-112, (**II**) SCaBER, and (**III**) T24 cells, and (**IV**) CLS cells normalized to control (n = 3); graphs show mean and biological replicates; statistical analysis was performed using one-way analysis of variance (ANOVA) with Dunnett post-hoc testing (***$p < 0.001$). Scale bar = 100 µm.

pro-apoptotic signaling, flow cytometric analysis of caspase 3/7 activity was performed (Fig. 2**d** representative for SCaBER cells) and found to be significantly increased, especially in the RT-112, SCaBER, and T24 cells (Fig. 2**e**). To monitor cell death on a more dynamic scale, quantitative kinetic fluorescence microscopy was performed. To track the appearance of terminally dead cells staining positive for DAPI and the relative intensity of mitotracker deep red, an indicator of intact mitochondria (Fig. 2**f;** top row RT-112, middle row T24, bottom row SCaBER). Onset of terminal cell death was observed early after gas plasma treatment within 6 h. Data were normalized to those of controls, indicating the fold-change increase of appearing $DAPI^+$ cells over time (Fig. 2**g**). Similarly, the mitochondrial staining showed a marked reduction in all tumor cell lines investigated (Fig. 2**h**). While cancer cell inactivation is the desired effect of any oncological therapy, tumor cell motility is less encouraged as it is a hallmark of cancer metastasis. Accordingly, the movement of individual cells was traced using time-lapse live-cell microscopy and algorithm-driven cell segmentation. Analyzing only viable ($DAPI^-$) cells, quantitative microscopy of the tumor cells' motility revealed a significant decline in SCaBER (II) and T24 cells (III) but not in RT-112 cells (I) (Fig. 2**i**).

*Gas plasma reduced 3D cancer spheroid viability and tumor burden in ovo*

Anti-tumor effects of medical gas plasma treatment were validated in three-dimensional tumor models. For this, spheroids of T24, RT-112, and SCaBER cells were generated (Fig. 3**a**). The three tumor cell lines formed appropriate 3D tumor spheroids, while the CLS cells did not, as seen by their flat and spread instead of

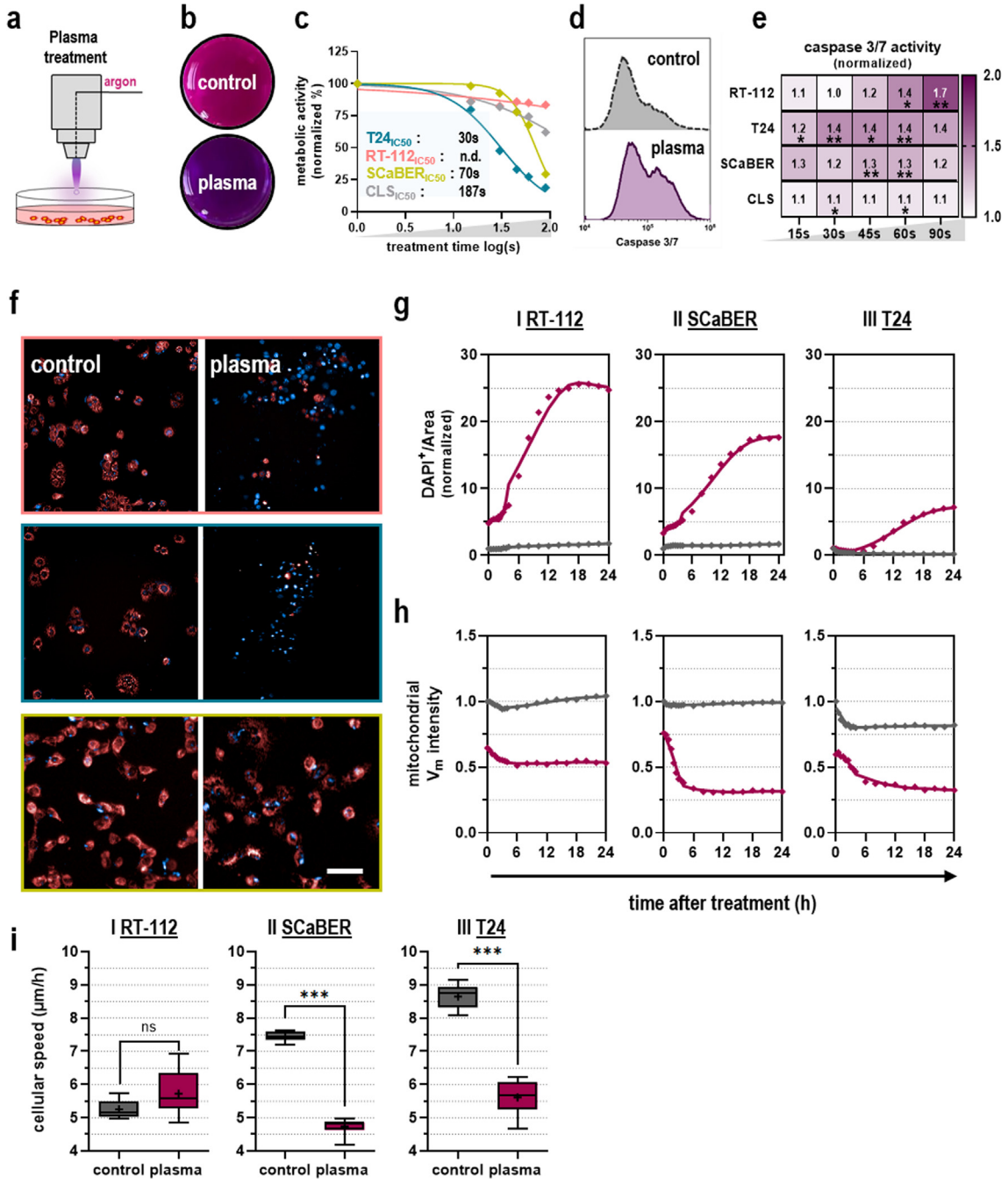


**Fig. 2. Gas plasma treatment reduced metabolic activity, motility, and viability in urothelial cancer cell lines.** (**a**) Schematic overview of gas plasma treatment performed in 2D *in vitro* experiments. (**b**) representative images of resazurin metabolization. (**c**) Metabolic activity quantification normalized to respective controls indicating $IC_{50}$ values (box) calculated from non-linear regression of log-transformed x-values (n = 8); graph shows mean. (**d**) Representative flow cytometry intensity histogram of caspase 3/7 activation. (**e**) Apoptosis quantification normalized to respective controls (n = 5); heat map shows mean; statistical analysis was performed using one-way analysis of variance (ANOVA) with Dunnett post-hoc testing (*p < 0.05, **p < 0.01; ***p < 0.001). (**f**) Representative images of DAPI and Mitotracker Red staining. (**g-h**) Quantification of (**g**) percent $DAPI^+$ cells and (**h**) mitochondrial membrane potential intensity evaluated until 24 h after gas plasma treatment normalized against the 0 h control (n = 3); graphs show mean. (**i**) 10–90 % percentile box plots (mean indicated by + ) showing quantification of cellular motility for (**I**) RT-112, (**II**) SCaBER, and (**III**) T24 cells (n = 3 with 5 technical replicates each); statistical analysis was performed using unpaired *t*-test (***p < 0.001). ns = non-significant. Scale bar = 100 µm (f).

compact appearance. Algorithm-based quantitative image analysis of dead tumor cells in spheroids and the 3D tumor spheroid size was performed (Fig. 3**b**). For the latter, a decline was found for RT-112 and SCaBER but not T24 cells following gas plasma exposure (Fig. 3**c**). The apparent increase seen with T24 cells was not due to growth but the spheroids falling apart due to cell death of outer cells, ultimately increasing the size determined by the software. In order to determine whether spheroid growth retardation seen with RT-112 and SCaBER cells was a consequence of either diminished cellular proliferation or tumor toxicity, sytox green (SG) staining was performed to label terminally dead cells. Quantification of SG intensity 24 h and 48 h after treatment revealed increased tumor toxicity with gas plasma treatment in all three bladder cancer cell lines (Fig. 3**d**).

This result was re-iterated in the hen's egg test of the chorioallantoic membrane (HET-CAM) model (Fig. 3**e**). Here, solid tumors

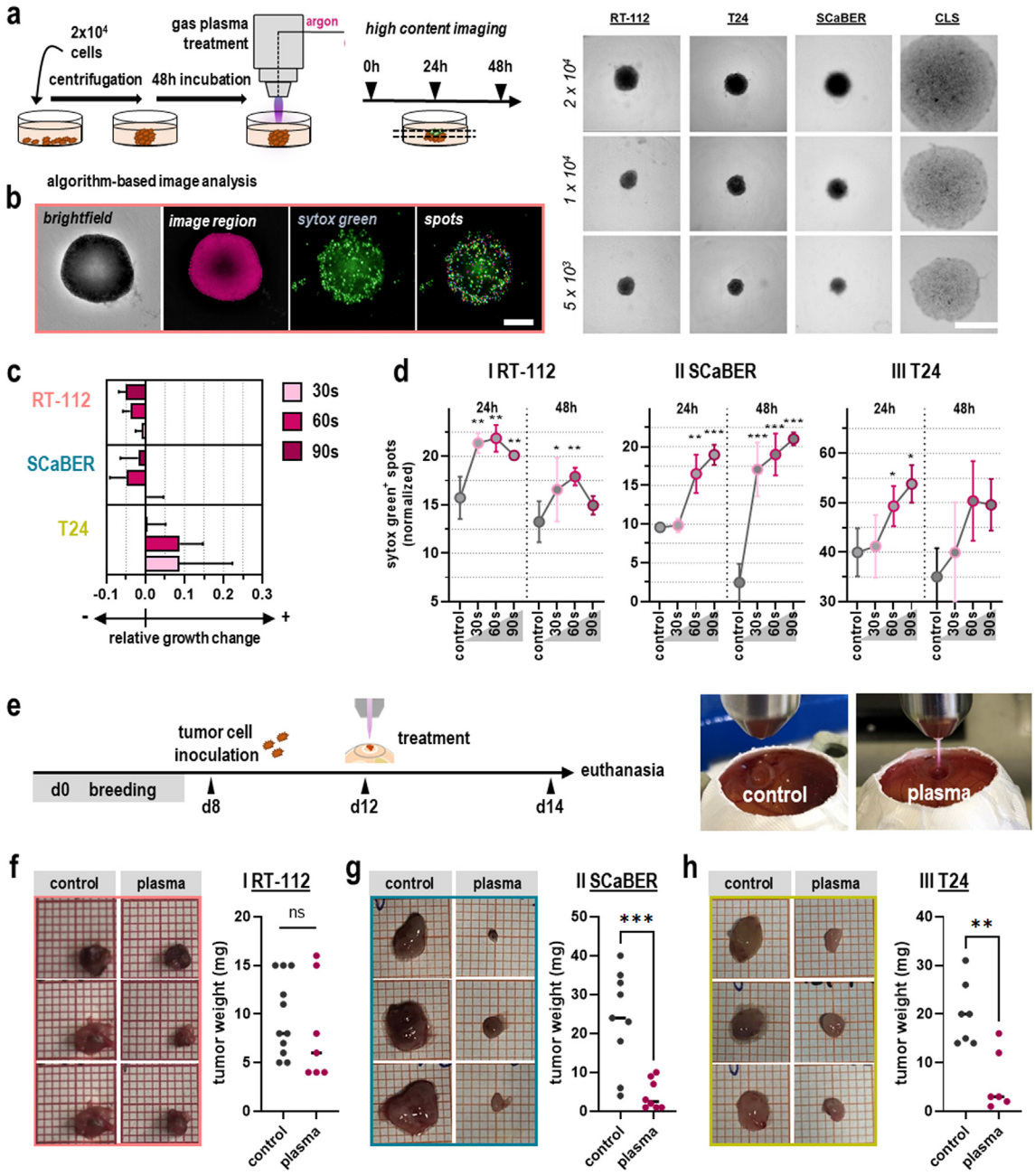


**Fig. 3. Gas plasma exposure elicits cytotoxicity in 3D urothelial cancer spheroids and vascularized tumor tissues in ovo.** (**a**) Schematic overview of the experimental 3D spheroid procedure and representative brightfield images of successful tumor spheroid formation of the tumor cell lines but not CLS cells. (**b**) Representative images of algorithm-based 3D tumor spheroid toxicity image analysis. (**c**) Relative growth change of urothelial cancer spheroids after gas plasma treatment compared to argon gas control (n = 3); bar graph shows mean ± standard error of the mean (SEM). (**d**) Quantification of sytox green-positive spots 24 h and 48 h after gas plasma treatment of (**I**) RT-112, (**II**) SCaBER, and (**III**) T24 spheroids; graphs show mean ± SEM; statistical analysis was performed using one-way analysis of variance (ANOVA) with Dunnett post-hoc testing (*p < 0.05, **p < 0.01; ***p < 0.001). (**e**) Schematic overview of in ovo experimental procedures (left) showing representative images of argon gas and gas plasma treatment performed in ovo (right). (**f–h**) Representative pictures of excised in ovo tumors followed by assessment of tumor weight of RT-112 (n = 11 (control), n = 8 (plasma); **f**), SCaBER (n = 9 (control), n = 8 (plasma); **g**), and T24 (n = 7 (control), n = 6 (plasma); **h**) cells; graphs show mean and biological replicates; statistical analysis was performed using unpaired *t*-test (**p < 0.01; ***p < 0.001). Scale bar = 100 μm (b).

are grown on the highly vascularized CAM of fertilized chicken eggs (*in ovo*). They perform neovascularization and stroma formation, recapitulating the tumor microenvironment to a greater extent than *in vitro* cell culture models in an *in-vivo*-like fashion. After an initial breeding period of seven days, T24, RT-112, and SCaBER cells were seeded on the CAM. They were exposed to gas plasma on day 10 after solid tumors had formed and compared to argon-treated control eggs. Tumor growth was examined by tumor weight 96 h later after careful tumor excision. While responses in RT-112 remained modest as in previous *in vitro* experiments (Fig. 3**f**), SCaBER (Fig. 3**g**) and T24 cells (Fig. 3**h**) vascularized tumors showed a significant decline in tumor weight following gas plasma exposure.

### *Medical gas plasma elicits apoptosis and changes gene expression signatures in ex vivo-treated human patient-derived bladder cancer samples*

Human urothelial carcinoma samples were obtained from eight patients undergoing transurethral tumor resection in the Clinic

and Polyclinic of Urology in Greifswald (Germany). Excised tumors were immediately prepared for *ex vivo* gas plasma treatment by cutting each sample into 5 mm pieces using standard pathology punch biopsies. Gas plasma treatment was performed for 60 s in conducting mode with direct contact between the gas plasma jet and target to maximize ROS/RNS delivery into the tissue. After an incubation period of 6 h, tumors were either cryo-embedded for subsequent tissue staining or snap-frozen using liquid nitrogen for longitudinal gene expression analysis (Fig. 4**a**). The patient collective in our study comprised 5 male and 3 female patients with a median age of 66 (Fig. 4**b**). The unequal gender ratio was expected as men are three times more likely to develop the disease. All samples were obtained from invasively growing high-grade tumors, as seen in representative computer tomography (CT) imaging of patients (Fig. 4**c**). TUNEL staining of tumor tissues revealed a significant increase in apoptotic cells in argon gas plasma-treated urinary bladder cancer tissue (Fig. 4**d**) but not in healthy urothelial tissue (Fig. 4**e**).

Subsequent whole transcriptome microarray analysis of human urothelial tumor tissues revealed pronounced alterations in gene expression signature 6 h after *ex vivo* plasma treatment (Fig. 5**a**). Among all differentially expressed genes (Fig. 5**b**), gene ontology (GO) classification showed several protein classes to be affected, with metabolite interconversion proteins, transcription factors, transmembrane signaling receptors, and transporter proteins belonging to the main categories (Fig. 5**c**). Sorting the differentially expressed genes for biological categories, cellular processes, metabolism, regulation, and response to stimulus were mainly affected (Fig. 5**d**). STRING network analysis moreover revealed several relationships between the targets regulated by gas plasma treatment (Fig. 5**e**). Of the 570 significantly regulated genes, about 200 coded for annotated proteins (Table 1). Among the top downregulated targets was the pro-oncogenic fibroblast growth factor receptor (FGFR), commonly overexpressed in urothelial cancer and highly related to tumor initiation and progression. Moreover, in line with augmented tumor toxicity observed in our study, apoptosis-inducing factor 2 (AIFm2), a redox-responsive protein involved in the p53-apoptosis signaling axis, was found to be highly upregulated in response to plasma treatment.

## Discussion

Medical gas plasma technology has proven its anti-tumor potential in multiple tumor entities *in vitro* and in vivo so far. This innovative treatment approach's principle relies on generating a versatile mix of ROS/RNS species capable of eliciting oxidative distress and thereby lethal damage in tumor cells. This concept is comparable to photodynamic therapy (PDT) that has already been implemented for many types of cancer therapies in clinical oncology [26] and is also under investigation for its usage in the treatment of urinary bladder cancer [27,28]. However, knowledge of the efficacy of the multi-ROS/RNS mixtures of medical gas plasma technology against this disease is rare.

Until now, a few studies investigated gas plasma-mediated tumor toxicity in urinary bladder cancer cells in 2D *in vitro* experiments [29,30] and a non-orthotopic xenograft mouse model [31]. In the present study, we characterized the tumor-toxic effects of medical gas plasma in four different human urinary bladder cancer lines with urothelial (RT-112, T24, CLS) and squamous differentiation (SCaBER) not only in 2D but also in 3D tumor models. For the first time, we investigated tumor growth of urinary bladder cancer cells in neovascularized tumors *in ovo* and found apoptosis-induction in human urinary carcinoma samples treated *ex vivo*. All gas plasma treatments were carried out using the kINPen MED. This plasma jet is accredited as a medical device in Europe and has shown promising results in the palliative treatment of head and neck cancer patients [32].

Following gas plasma exposure of bladder cancer cells *in vitro*, we observed reduced metabolic activity and motility in all tumor cell lines. Estimating an individual decrease in metabolic activity by assessing NADPH levels could also imply a global reduction in viable cell count, especially in toxic regimens. Correlation analysis revealed a moderate but significant correlation between resorufin fluorescence and live-cell counts (**Figure S1a**), raising the question of distinguishing between a tumor toxic or tumor static action. Induction of irreversible cell death signaling was confirmed in all tumor cell lines and was accompanied by signs of apoptotic cell death signaling such as caspase 3/7 activation, which is in line with previous findings [33,34]. Excessive ROS/RNS exposure, as generated in medical gas plasmas, can elicit endoplasmatic reticulum (ER) stress resulting in calcium influx into the mitochondria and mitochondria-dependent pro-apoptotic signaling [35,36]. This requires a reduction in mitochondrial membrane potential early on, as observed in time-lapse microscopy experiments in our study. Along similar lines, an increase of pro-apoptotic Bax over Bcl-2 [37] and mitochondrial release of cytochrome *C* [38] were reported before in response to gas plasma treatment. However, considering heterogeneous and cell-type-specific death responses, attributing ROS-induced cell death to a particular modality is complex [39], but apoptosis is the most commonly observed type of cell death across a vast number of plasma medicine studies in the past 15 years.

Additionally, pronounced tumor-toxic gas plasma effects were not only observed in 2D *in vitro* experiments but also in more complex tumor models, namely 3D tumor spheroids, vascularized *in ovo* tumors, and *ex vivo* treated human tumor samples, emphasizing gas plasma to be a promising oncological approach to tackle urinary bladder cancer. Gene expression profiling of *ex vivo* treated human urothelial cancer tissue was performed to investigate signaling responses and molecular pathways underlying the observed anti-tumor effects. Gas plasma treatment resulted in the downregulation of FGFR3 (fibroblast growth factor receptor 3) expression, which is amplified in several cancers, including urothelial carcinoma. Under physiological conditions, ligand binding of fibroblast growth factor (FGF) plays a central role in metabolism, tissue homeostasis, cell migration, and survival. However, oncogenic dysregulation of the FGF/FGFR signaling axis is associated with accelerated tumor progression and aggravates disease prognosis [40]. Targeting FGF/FGFR signaling using FGFR inhibitors, such as Erdafitinib, has already shown beneficial results in treating adult patients suffering from locally advanced or metastatic bladder cancer with FGFR3 mutations [41]. Along similar lines, downregulation of FGFR3 expression might thereby contribute to gas plasma-mediated anti-tumor effects. Impaired tumor progression due to reduced tumor cell proliferation was additionally accompanied by induction of pro-apoptotic signaling pathways. Differential gene expression analysis revealed upregulation of redox-responsive AIFm2, a p53 target that plays a central role in caspase-independent apoptosis induction and is localized in mitochondria in healthy cells [42–44]. Upon pro-apoptotic oxidative stress conditions, nuclear translocation of AIFm2 takes place, resulting in chromatin condensation and DNA fragmentations [45–47].

Gas plasma-mediated tumor toxicity is mainly attributed to reactive species first generated in the plasma gas phase. The contribution of other gas plasma properties, such as electrical fields and UV radiation, is believed to be of lesser importance to the biomedical observed [15]. Gas phase species comprise, for instance, reactive species such as hydroxyl radicals ($^{\cdot}OH$), atomic oxygen (O), superoxide ($O_2^{\cdot-}$), and nitric oxide (NO) and can be partially influenced by changes in feed gas composition. *In vitro*, however, where

a

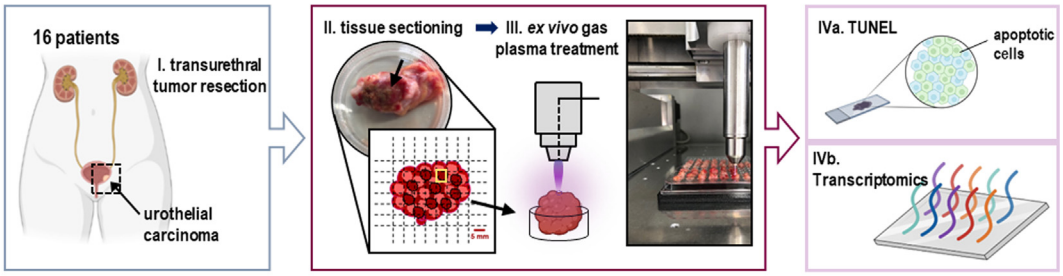


b

| Patient cohort | |
|---|---|
| Characteristic | Number |
| Gender, n (%) | |
| Male | 9 (56,3) |
| Female | 7 (43.7) |
| Age, years | |
| Median | 69 (±7.31) |
| Range | 52-79 |
| Grade, n (%) | |
| Low | 0 (0) |
| Intermediate | 1 (6,2) |
| High | 15 (93,8) |

c

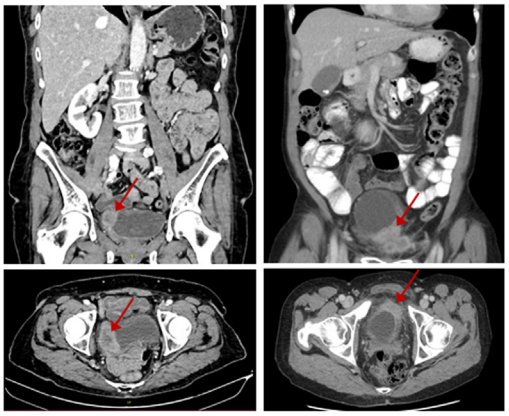

d

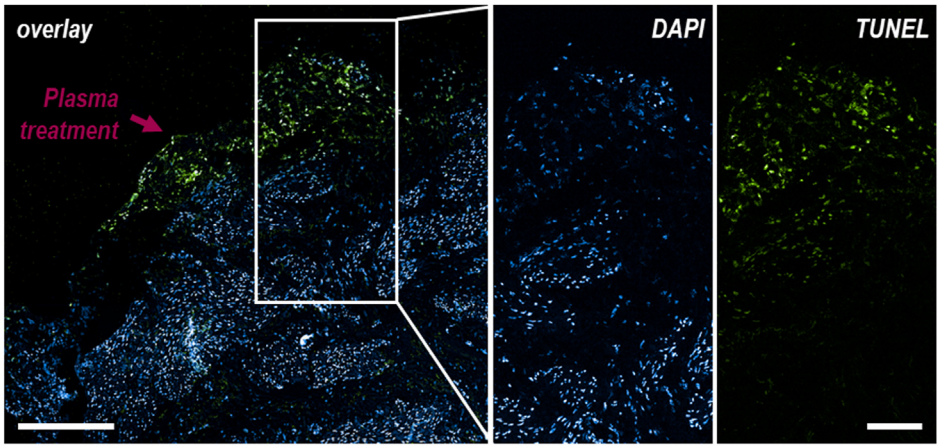


e

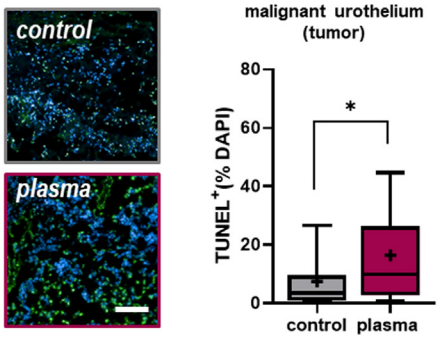


f

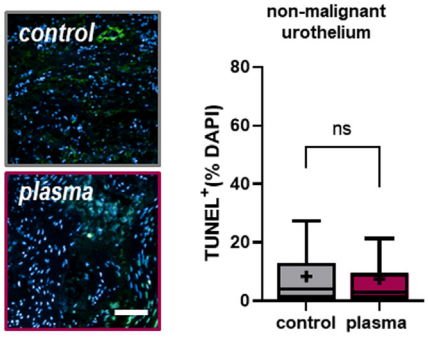


**Fig. 4. Gas plasma treatment induces apoptosis in human urothelial cancer tissues ex vivo.** (**a**) Schematic overview of study design (created with biorender.com). (**b**) Urothelial cancer patient characteristics. (**c**) Representative computer tomography (CT) images of patients suffering from urinary bladder cancer and muscle-invasive growing tumors are indicated by red arrows. (**d**) Representative TUNEL images of human urothelial carcinoma samples and healthy urothelial tissue. (**e**) 5–95 percentile boxplots (mean indicated by + ) of the percentage of TUNEL$^+$ cells among all nuclei (DAPI$^+$) in malignant urothelial tissue (tumor; n = 16); statistical analysis was performed using *t*-test (*p < 0.05). (**f**) 5–95 percentile boxplots (mean indicated by + ) of the percentage of TUNEL$^+$ cells among all nuclei (DAPI$^+$) in non-malignant urothelial tissue (healthy controls; n = 16); statistical analysis was performed using *t*-test. ns = non-significant. Scale bar = 100 μm (d).

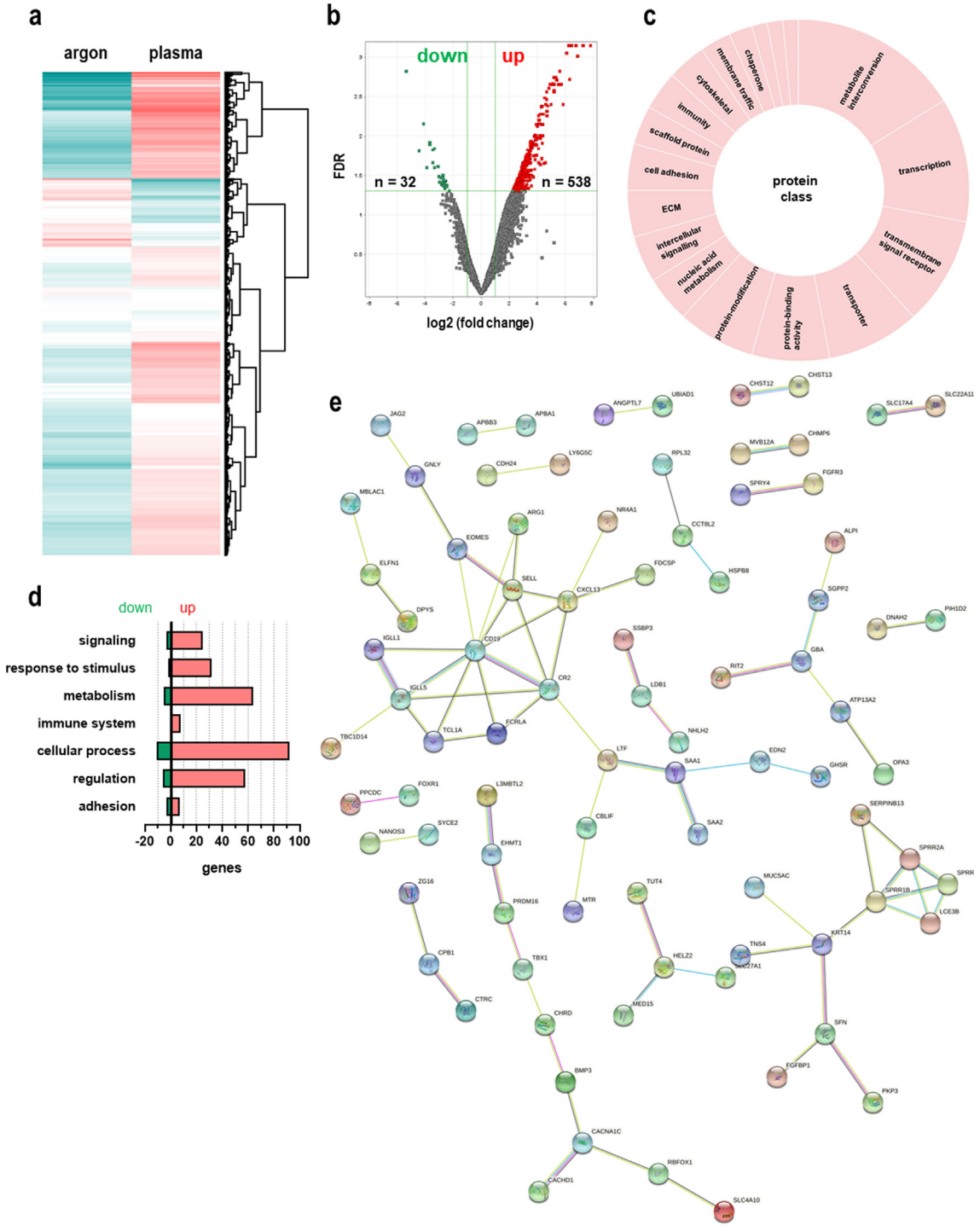


**Fig. 5. Gas plasma treatment alters gene expression profile in human urothelial cancer tissues ex vivo.** (**a-b**) Weighted pair group method with arithmetic mean (WPGMA) hierarchical clustering of house-keeping (GAPDH)-normalized gene expression values in human urothelial cancer tissues after ex vivo plasma treatment compared to argon treated controls (**a**) and volcano plot showing significantly down (green) and up (red) regulated genes (**b**). (**c-d**) Gene ontology (GO) protein classification (**c**) and classification of biological processes corresponding to differentially expressed genes after ex vivo plasma treatment (**d**). (**e**) STRING network analysis showing all significantly regulated targets with at least one interaction partner being also significantly regulated. The dendrogram of hierarchical clustering is log-scaled. FDR = false discovery rate. ECM = extracellular matrix.

cells are mainly surrounded by bulk liquids such as cell culture media, the high reactivity of those species leads to fast deterioration to a few long-lived species in the liquid phase [48,49]. Here, $H_2O_2$ is thought to play a significant role in gas plasma-mediated toxicity [50]. At the same time, comparison of concentration-matched $H_2O_2$ levels with gas plasma treatment in more complex and thereby physiologically more relevant cell culture models revealed the latter to outperform the former regarding tumor-toxic effects [51], indicating that other species might play a role. Among them, synergies between $H_2O_2$ and $NO_2^-$ are discussed [52].

Dichlorofluorescein fluorescence used in our study as an intracellular ROS indicator is known to be highly dependent on the intracellular oxidase activity rather than ROS levels [53]. The central role of gas plasma-derived ROS in providing biomedical effects

**Table 1**
Differentially expressed genes of whole gene expression transcriptomic profiling of gas plasma-treated human urothelial cancer tissues with at least a twofold increase or decrease. The table is sorted for up and downregulation and fold-changes (FC) in expression.

| Gene | FDR | regulation | $log_2$(FC) | Gene | FDR | regulation | $log_2$(FC) |
|---|---|---|---|---|---|---|---|
| TMEM200C | 2.83 | down | −5.36 | GNLY | 1.34 | up | 2.41 |
| FGFBP1 | 2.15 | down | −4.13 | GBA | 1.37 | up | 2.41 |
| KLHDC7B | 1.60 | down | −3.89 | RNF225 | 1.33 | up | 2.41 |
| TBX1 | 1.92 | down | −3.67 | APBB3 | 1.35 | up | 2.42 |
| ANXA8L1 | 1.66 | down | −3.44 | SFTPA1 | 1.36 | up | 2.43 |
| BTBD16 | 1.84 | down | −3.36 | PIP5K1A | 1.38 | up | 2.45 |
| SFN | 1.60 | down | −3.34 | LAIR1 | 1.36 | up | 2.45 |
| PKP3 | 1.62 | down | −3.09 | CAP2 | 1.38 | up | 2.45 |
| SPRR2D | 1.49 | down | −3.03 | KLHL6 | 1.34 | up | 2.45 |
| ANGPTL7 | 1.42 | down | −3.00 | NPAS3 | 1.34 | up | 2.48 |
| KLHDC7B | 1.47 | down | −2.92 | LRRD1 | 1.36 | up | 2.48 |
| PADI1 | 1.38 | down | −2.81 | CTRC | 1.34 | up | 2.49 |
| GJB4 | 1.47 | down | −2.81 | ALPI | 1.32 | up | 2.49 |
| LY6D | 1.40 | down | −2.80 | OR5H1 | 1.40 | up | 2.50 |
| TNS4 | 1.42 | down | −2.76 | PCDHGA3 | 1.38 | up | 2.50 |
| SPRR2A | 1.47 | down | −2.75 | MBLAC1 | 1.37 | up | 2.50 |
| TUT4 | 1.47 | down | −2.75 | PDILT | 1.33 | up | 2.51 |
| AQP3 | 1.51 | down | −2.74 | CXCL13 | 1.43 | up | 2.51 |
| KRT14 | 1.37 | down | −2.70 | SELL | 1.30 | up | 2.51 |
| CLDN1 | 1.44 | down | −2.63 | PRDM16 | 1.36 | up | 2.52 |
| TENM2 | 1.44 | down | −2.62 | TMEM241 | 1.43 | up | 2.52 |
| EDN2 | 1.34 | down | −2.59 | PPCDC | 1.43 | up | 2.53 |
| IL20RB | 1.44 | down | −2.58 | RASD2 | 1.40 | up | 2.53 |
| PAGE2 | 1.43 | down | −2.53 | RPL32 | 1.39 | up | 2.53 |
| FGFR3 | 1.36 | down | −2.49 | SLC30A2 | 1.33 | up | 2.54 |
| SPRR1B | 1.38 | down | −2.45 | SNORA60 | 1.36 | up | 2.56 |
| TMPRSS4 | 1.31 | down | −2.27 | SRGAP1 | 1.38 | up | 2.57 |
| SLC22A7 | 1.30 | up | 2.24 | PRDM13 | 1.40 | up | 2.57 |
| NPBWR1 | 1.32 | up | 2.27 | PCARE | 1.43 | up | 2.57 |
| CCT8L2 | 1.33 | up | 2.32 | EHMT1 | 1.44 | up | 2.58 |
| SGPP2 | 1.32 | up | 2.33 | TSGA13 | 1.31 | up | 2.59 |
| REP15 | 1.33 | up | 2.33 | GCLM | 1.30 | up | 2.61 |
| CBLIF | 1.32 | up | 2.34 | NR4A1 | 1.46 | up | 2.62 |
| NANOS3 | 1.33 | up | 2.34 | ANKRD63 | 1.39 | up | 2.63 |
| CHST13 | 1.34 | up | 2.34 | FCRLA | 1.46 | up | 2.63 |
| ARG1 | 1.34 | up | 2.35 | SMIM10L2A | 1.46 | up | 2.63 |
| OLIG3 | 1.30 | up | 2.35 | RPS6KA1 | 1.46 | up | 2.63 |
| COL9A1 | 1.36 | up | 2.36 | TAS2R13 | 1.34 | up | 2.64 |
| TMEM178B | 1.35 | up | 2.38 | LTF | 1.36 | up | 2.64 |
| SLC4A10 | 1.30 | up | 2.39 | OPA3 | 1.37 | up | 2.65 |
| JAG2 | 1.36 | up | 2.39 | FAM107A | 1.44 | up | 2.66 |
| HMX3 | 1.37 | up | 2.40 | OR10P1 | 1.33 | up | 2.66 |
| GPR160 | 1.33 | up | 2.40 | VSIG10L2 | 1.34 | up | 2.66 |
| **Gene** | **FDR** | **regulation** | **$log_2$(FC)** | **Gene** | **FDR** | **regulation** | **$log_2$(FC)** |
| XAGE-4 | 1.38 | up | 2.66 | DPYS | 1.32 | up | 2.93 |
| ODF3L2 | 1.43 | up | 2.67 | LRRC2 | 1.57 | up | 2.95 |
| CHST12 | 1.37 | up | 2.67 | EOMES | 1.40 | up | 2.95 |
| SLC26A1 | 1.43 | up | 2.67 | SCARNA3 | 1.66 | up | 2.96 |
| OR4S1 | 1.38 | up | 2.68 | NANOS2 | 1.62 | up | 2.97 |
| IGLL5 | 1.44 | up | 2.69 | RSPH1 | 1.40 | up | 2.97 |
| BMP3 | 1.50 | up | 2.69 | SNORA59B | 1.32 | up | 2.97 |
| CD19 | 1.45 | up | 2.70 | COL20A1 | 1.54 | up | 2.98 |
| SPOCK2 | 1.47 | up | 2.70 | ELFN1 | 1.62 | up | 2.99 |
| OR1J1 | 1.41 | up | 2.70 | PPP1R11 | 1.66 | up | 3.00 |
| CTRC | 1.46 | up | 2.71 | RIT2 | 1.59 | up | 3.02 |
| SV2C | 1.47 | up | 2.71 | IGLL1 | 1.50 | up | 3.03 |
| CST6 | 1.34 | up | 2.71 | PLEKHG4B | 1.52 | up | 3.03 |
| DET1 | 1.43 | up | 2.71 | FAT2 | 1.51 | up | 3.03 |
| LCE3B | 1.43 | up | 2.71 | DYNC2LI1 | 1.57 | up | 3.05 |
| COMMD7 | 1.46 | up | 2.72 | SLC25A47 | 1.61 | up | 3.06 |
| AIF1L | 1.44 | up | 2.72 | GOLGA7B | 1.44 | up | 3.06 |
| MUC5AC | 1.43 | up | 2.73 | BTN2A1 | 1.66 | up | 3.09 |
| SPATA9 | 1.33 | up | 2.74 | CPB1 | 1.36 | up | 3.11 |
| TAF1L | 1.44 | up | 2.75 | CNP | 1.59 | up | 3.12 |
| CACNA1C | 1.52 | up | 2.76 | PRPF40B | 1.60 | up | 3.12 |
| OVOS2 | 1.45 | up | 2.76 | RNF24 | 1.54 | up | 3.13 |
| ACP4 | 1.43 | up | 2.77 | STK16 | 1.66 | up | 3.14 |
| TBC1D14 | 1.50 | up | 2.78 | ATP13A2 | 1.74 | up | 3.19 |
| FAM47A | 1.51 | up | 2.78 | TCL1A | 1.49 | up | 3.22 |
| SPRY4 | 1.44 | up | 2.78 | CYP4Z1 | 1.57 | up | 3.28 |
| DDO | 1.50 | up | 2.78 | MMP28 | 1.76 | up | 3.31 |
| DNPEP | 1.44 | up | 2.78 | SLC27A1 | 1.83 | up | 3.31 |
| PCDH19 | 1.45 | up | 2.79 | UBIAD1 | 1.68 | up | 3.34 |

(*continued on next page*)

**Table 1** (*continued*)

| Gene | FDR | regulation | $log_2$(FC) | Gene | FDR | regulation | $log_2$(FC) |
|---|---|---|---|---|---|---|---|
| HSPB8 | 1.50 | up | 2.79 | SLC22A11 | 1.71 | up | 3.36 |
| SLC17A4 | 1.54 | up | 2.79 | SPATA1 | 1.83 | up | 3.39 |
| RNU105C | 1.35 | up | 2.79 | RETREG2 | 1.67 | up | 3.40 |
| XRCC3 | 1.45 | up | 2.82 | CCDC66 | 1.70 | up | 3.40 |
| DNAH2 | 1.54 | up | 2.83 | ANKRD30A | 1.66 | up | 3.44 |
| CHMP6 | 1.44 | up | 2.86 | HELZ2 | 1.71 | up | 3.48 |
| NHLH2 | 1.44 | up | 2.87 | ALKAL2 | 1.46 | up | 3.49 |
| CDH24 | 1.58 | up | 2.87 | ZG16 | 1.82 | up | 3.49 |
| NT5DC4 | 1.51 | up | 2.87 | MTR | 1.92 | up | 3.50 |
| ANKRD20A2 | 1.51 | up | 2.89 | SYCE2 | 1.66 | up | 3.53 |
| TMEM40 | 1.61 | up | 2.89 | IL36B | 1.86 | up | 3.55 |
| MRAP | 1.42 | up | 2.89 | SAA1 | 1.57 | up | 3.55 |
| MEGF11 | 1.54 | up | 2.91 | SAA2 | 1.37 | up | 3.56 |
| CHRD | 1.58 | up | 2.93 | SERPINB13 | 1.89 | up | 3.58 |
| XAGE-4 | 1.38 | up | 2.66 | DPYS | 1.32 | up | 2.93 |
| ODF3L2 | 1.43 | up | 2.67 | LRRC2 | 1.57 | up | 2.95 |
| **Gene** | **FDR** | **regulation** | **$log_2$(FC)** | **Gene** | **FDR** | **regulation** | **$log_2$(FC)** |
| GRAMD1B | 1.85 | up | 3.64 | RBFOX1 | 1.64 | up | 4.22 |
| EDA | 1.89 | up | 3.65 | MED15 | 2.37 | up | 4.24 |
| TSHB | 1.92 | up | 3.68 | AIFm2 | 1.91 | up | 4.35 |
| USP30 | 1.47 | up | 3.71 | CR2 | 2.15 | up | 4.36 |
| GPR78 | 1.75 | up | 3.74 | PIH1D2 | 2.01 | up | 4.37 |
| SNORA71B | 2.00 | up | 3.76 | TAS2R19 | 1.66 | up | 4.46 |
| TEX37 | 2.00 | up | 3.83 | TMCC2 | 1.67 | up | 4.56 |
| PDXK | 1.95 | up | 3.85 | ISLR2 | 2.47 | up | 4.64 |
| FDCSP | 1.88 | up | 3.88 | GLYAT | 2.66 | up | 4.92 |
| SULT6B1 | 1.76 | up | 3.91 | LDB1 | 2.66 | up | 5.01 |
| CACHD1 | 1.98 | up | 3.91 | PCDH11X | 2.66 | up | 5.20 |
| MIR100HG | 2.00 | up | 3.93 | GHSR | 2.75 | up | 5.24 |
| L3MBTL2 | 1.76 | up | 3.93 | EXOC1L | 2.66 | up | 5.48 |
| SSBP3 | 2.12 | up | 3.99 | LY6G5C | 2.66 | up | 5.49 |
| OTOG | 1.84 | up | 4.06 | ST18 | 2.40 | up | 5.82 |
| MIR100HG | 2.20 | up | 4.06 | OR6Y1 | 3.15 | up | 6.23 |
| APBA1 | 2.26 | up | 4.06 | TSPAN32 | 3.15 | up | 6.44 |
| FOXR1 | 1.98 | up | 4.10 | MRTFB | 3.01 | up | 6.86 |

is undisputed, nevertheless [15]. For instance, similar intensity electrical fields and UV radiation do not recapitulate gas plasma effects [54], and ROS scavengers such as catalase [55], glutathione [35], and NAC [51] attenuate gas plasma-mediated effects. A substantial ROS impact on fatty acid chains yields cleavages and a decreased membrane stiffness [56], which was suggested to facilitate further ROS entry into the cells. This is further supported if cells exhibit low membrane cholesterol [57]. In addition, some members of the aquaporin (AQ) channel family, e.g., AQP1, AQP3, AQP8, and AQP9, are also known to transport $H_2O_2$ across the cell membrane [58]. Moreover, cell lines that display an altered redox metabolism, e.g., if having constitutive access to cysteine for GSH biosynthesis, have been shown to be more resistant to gas plasma exposure [19]. Finally, indirect means of intracellular oxidant-antioxidant perturbations have been reported, e.g., by assessing thiol content [59], mitochondrial superoxide [60], and lipid peroxidation [61]. Notwithstanding, it is conceivable that mitochondrial dysfunction had interfered with the measured DCF fluorescence signal at later time points in this study as cytochrome *c* is known to possess a catalytic role in DCF oxidation [62,63]. In the light of the many studies underlining the central role of ROS, we continue to suggest lethal oxidative damage to be the underlying principle in plasma oncology.

An emerging challenge in clinical oncology is inherent or acquired therapy resistance, which may also impair the efficacy of medical gas plasma therapy. In our study, the extent of cell death markedly differed between the tumor cell lines investigated, showing the lowest response in low-grade RT-112 cells grown *in ovo*. Unfortunately, investigating a suitable non-malignant cell line of respective tumor entities as a comparator is often not feasible. Despite being recognized as tumor cell line, the CLS-439 cells used for comparison in our study show several characteristics of low malignancy. Compared to the three other cell lines, CLS-439 did not form spheroids (Fig. 3**a**) or grew on the CAM chicken embryos (Fig. 3**f**) as malignant cells usually do, also in the current study. CLS-439 also did not form colonies in the colony-formation assay in agar (**Fig. S1c**) and had the by far slowest doubling time (**Fig. S1b**) across all cell lines in this study (and also compared to most other proper tumor cell lines as the NCI-60 [64]). A comparable case is HaCaT keratinocytes which is widely used in the literature as non-malignant cell line to compare against tumor cells, even in non-skin cancer models, albeit some reports have suggested a low degree of malignancy also in these cells [65,66]. Irrespective of this, recent research indicates that the suggested selectivity of gas plasma treatment towards malignant cells is also dependent on the tumor cell line investigated and the cell line used for comparison [67–69], suggesting characteristics other than malignancy to contribute to sensitivity to gas plasma exposure, such as metabolic activity. In line with our previous study [70], Pearson analysis revealed a good correlation between basal metabolic activity and cell line sensitivity in our study as well (**Fig. S2a**). Additionally, membrane cholesterol content and expression of ROS/RNS producing enzymes, namely NOX3 and NOS3, might play a role.

In our study, the transcript of apoptosis-inducing factor mitochondrial 2 (AIFm2) was significantly increased in gas plasma-treated urothelial cancer tissue. The factor is known to be critical in caspase-independent apoptosis [71], which is incongruent with our *in vitro* results on caspase-dependent apoptosis. At the same time, AIF was also described to be involved in caspase-dependent

cell death [72] and, moreover, is redox-regulated through thioredoxin [73]. Hence, the regulation of this factor might be subject to redox control, and gas plasma-derived ROS/RNS of the kINPen can act on redox-regulating factors *in vitro* and in vivo [74,75]. Recent evidence added another critical function to AIFM2, which was renamed FSP1, namely, its critical role in protecting cells from lipid peroxidation-induced ferroptosis [76]. In the light of the many short-lived reactive species being released onto the tumor tissue by gas plasma exposure, it is conceivable that lipid oxidation occurs as *in vitro* and in silico studies suggested before [57,61,77,78], although we cannot provide direct evidence of lipid peroxidation and ferroptosis in the current study.

Despite the promising nature of our results, a significant problem in the clinical treatment of urinary bladder cancer is high recurrence rates even after pathologically confirmed R0 resection. Patients suffering from non-invasive urinary bladder cancer benefit from instillation therapy with Bacillus Calmette-Guérin (BCG), a live-attenuated strain of *Mycobacterium tuberculosis* [79]. Here, an anti-tumor immune response is initiated, reducing the risk of tumor recurrence by creating immune memory. Our study focused on tumor toxicity after gas plasma treatment in multiple tumor models without regard to tumor immunogenicity and following tumor-immune cell interaction. In several other tumor entities, gas plasma treatment has already shown its potential to increase tumor cell immunogenicity resulting in increased infiltration of antigen-presenting cells and lymphocytes into the tumor microenvironment (TME) [24,80–83]. In the future, the potential of gas plasma to enhance anti-tumor immunity in urinary bladder cancer has to be investigated. Collectively, our study suggests medical gas plasma treatment to be a promising therapeutic approach for treating urothelial carcinoma selectively.

## Conclusion

We investigated the anti-tumor effects of medical gas plasma exposure in four human bladder cancer cell lines in 2D and 3D cell culture models and tumor spheroids, neovascularized *in ovo* tumors, and patient-derived primary cancer tissue being gas plasma-treated *ex vivo*. Regarding the need to develop new therapeutic options for urinary bladder cancer, medical gas plasma technology represents a promising tool for slowing tumor growth in urinary bladder carcinomas in future clinical applications, especially if applied via urethrocystoscopy.

## CRediT authorship contribution statement

**Nadine Gelbrich:** Data curation, Formal analysis, Project administration, Resources, Validation, Writing – original draft. **Lea Miebach:** Data curation, Formal analysis, Investigation, Methodology, Software, Validation, Visualization, Writing – original draft. **Julia Berner:** Data curation, Formal analysis, Writing – review & editing. **Eric Freund:** Data curation, Formal analysis, Investigation, Methodology, Software, Writing – review & editing. **Fariba Saadati:** Formal analysis, Software, Writing – review & editing. **Anke Schmidt:** Data curation, Formal analysis, Investigation, Methodology, Writing – review & editing. **Matthias Stope:** Funding acquisition, Writing – review & editing. **Uwe Zimmermann:** Resources, Writing – review & editing. **Martin Burchardt:** Funding acquisition, Resources, Writing – review & editing. **Sander Bekeschus:** Conceptualization, Funding acquisition, Investigation, Methodology, Project administration, Resources, Software, Supervision, Writing – original draft, Writing – review & editing.

## Declaration of Competing Interest

The authors declare that they have no known competing financial interests or personal relationships that could have appeared to influence the work reported in this paper.

## Acknowledgments

Technical support by Felix Niessner (INP) and Henry Skowski (INP) is gratefully acknowledged.

## Funding

This study was funded by the German Federal Ministry of Education and Research (BMBF), grant numbers 03Z22DN11 and 03Z22Di1 to SB, and as well as the Ferdinand-Eisenberger-Founda tion (Germany), grant number GeN1FE-20 to NG and SB.

## Compliance with Ethics requirements

Primary urothelial carcinoma tissue of the renal pelvis and urinary bladder was obtained from patients undergoing nephrectomy or cystectomy in the Clinic and Polyclinic for Urology Greifswald under the approval of the local ethics committee (approval number: BB 144/19a) and patients' informed consent.

## References

[1] Witjes JA et al. Eau-esmo consensus statements on the management of advanced and variant bladder cancer-an international collaborative multistakeholder effort(dagger): Under the auspices of the eau-esmo guidelines committees. Eur Urol 2020;77:223–50. doi: https://doi.org/10.1016/j.eururo.2019.09.035.
[2] Bray F et al. Global cancer statistics 2018: Globocan estimates of incidence and mortality worldwide for 36 cancers in 185 countries. CA Cancer J Clin 2018;68:394–424. doi: https://doi.org/10.3322/caac.21492.
[3] Babjuk M et al. European association of urology guidelines on non-muscle-invasive bladder cancer (tat1 and carcinoma in situ) - 2019 update. Eur Urol 2019;76:639–57. doi: https://doi.org/10.1016/j.eururo.2019.08.016.
[4] Martincorena I et al. Somatic mutation in cancer and normal cells. Science 2015;349:1483–9. doi: https://doi.org/10.1126/science.aab4082.
[5] Lei AQ et al. Current treatment of metastatic bladder cancer and future directions. Expert Rev Anticancer Ther 2011;11:1851–62. doi: https://doi.org/10.1586/era.11.181.
[6] Tanji N et al. Long-term results of combined chemotherapy with gemcitabine and cisplatin for metastatic urothelial carcinomas. Int J Clin Oncol 2010;15:369–75. doi: https://doi.org/10.1007/s10147-010-0069-2.
[7] Tan WS et al. Management of non-muscle invasive bladder cancer: A comprehensive analysis of guidelines from the united states, europe and asia. Cancer Treat Rev 2016;47:22–31. doi: https://doi.org/10.1016/j.ctrv.2016.05.002.
[8] Comperat EM et al. Grading of urothelial carcinoma and the new "world health organisation classification of tumours of the urinary system and male genital organs 2016". Eur Urol Focus 2019;5:457–66. doi: https://doi.org/10.1016/j.euf.2018.01.003.
[9] Soukup V et al. Follow-up after surgical treatment of bladder cancer: A critical analysis of the literature. Eur Urol 2012;62:290–302. doi: https://doi.org/10.1016/j.eururo.2012.05.008.
[10] Mari, A., *et al.* Genetic determinants for chemo- and radiotherapy resistance in bladder cancer. *Transl Androl Urol* **2017**, *6*, 1081-1089, 10.21037/tau.2017.08.19.
[11] Dobruch J et al. Gender and bladder cancer: A collaborative review of etiology, biology, and outcomes. Eur Urol 2016;69:300–10. doi: https://doi.org/10.1016/j.eururo.2015.08.037.
[12] Hauner K et al. side effects of chemotherapy. Urologe A 2017;56:472–9. doi: https://doi.org/10.1007/s00120-017-0338-z.
[13] Schardt J et al. Forty years of cisplatin-based chemotherapy in muscle-invasive bladder cancer: Are we understanding how, who and when? World J Urol 2019;37:1759–65. doi: https://doi.org/10.1007/s00345-018-2544-8.
[14] Dai X et al. The emerging role of gas plasma in oncotherapy. Trends Biotechnol 2018;36:1183–98. doi: https://doi.org/10.1016/j.tibtech.2018.06.010.
[15] Privat-Maldonado A et al. Ros from physical plasmas: Redox chemistry for biomedical therapy. Oxid Med Cell Longev 2019;2019:9062098. doi: https://doi.org/10.1155/2019/9062098.
[16] Fluhr JW et al. In vivo skin treatment with tissue-tolerable plasma influences skin physiology and antioxidant profile in human stratum corneum. Exp

Dermatol 2012;21:130–4. doi: https://doi.org/10.1111/j.1600-0625.2011.01411.x.
[17] Sies H et al. Reactive oxygen species (ros) as pleiotropic physiological signalling agents. Nat Rev Mol Cell Biol 2020;21:363–83. doi: https://doi.org/10.1038/s41580-020-0230-3.
[18] Kang SU et al. Nonthermal plasma induces head and neck cancer cell death: The potential involvement of mitogen-activated protein kinase-dependent mitochondrial reactive oxygen species. Cell Death Dis 2014;5:e1056.
[19] Bekeschus S et al. Xct (slc7a11) expression confers intrinsic resistance to physical plasma treatment in tumor cells. Redox Biol 2020;30:. doi: https://doi.org/10.1016/j.redox.2019.101423101423.
[20] Weiss M et al. Cold atmospheric plasma treatment induces anti-proliferative effects in prostate cancer cells by redox and apoptotic signaling pathways. PLoS ONE 2015;10:e0130350.
[21] Weiss M et al. Physical plasma: A new treatment option in gynecological oncology. Arch Gynecol Obstet 2018;298:853–5. doi: https://doi.org/10.1007/s00404-018-4889-z.
[22] Bekeschus, S., *et al.* Basic research in plasma medicine - a throughput approach from liquids to cells. *J Vis Exp* **2017**, e56331, 10.3791/56331.
[23] Reuter S et al. The kinpen-a review on physics and chemistry of the atmospheric pressure plasma jet and its applications. J Phys D: Appl Phys 2018;51. doi: https://doi.org/10.1088/1361-6463/aab3ad.
[24] Bekeschus S et al. Medical gas plasma jet technology targets murine melanoma in an immunogenic fashion. Adv Sci (Weinh) 2020;7:1903438. doi: https://doi.org/10.1002/advs.201903438.
[25] Bekeschus S et al. Risk assessment of kinpen plasma treatment of four human pancreatic cancer cell lines with respect to metastasis. Cancers (Basel) 2019;11:1237. doi: https://doi.org/10.3390/cancers11091237.
[26] Morton CA et al. A randomized, multinational, noninferiority, phase iii trial to evaluate the safety and efficacy of bf-200 aminolaevulinic acid gel vs. Methyl aminolaevulinate cream in the treatment of nonaggressive basal cell carcinoma with photodynamic therapy. Br J Dermatol 2018;179:309–19. doi: https://doi.org/10.1111/bjd.16441.
[27] Rosenzweig B et al. Neoadjuvant vascular-targeted photodynamic therapy improves survival and reduces recurrence and progression in a mouse model of urothelial cancer. Sci Rep 2021;11:4842. doi: https://doi.org/10.1038/s41598-021-84184-y.
[28] Corradi RB et al. Effectiveness of the combination of vascular targeted photodynamic therapy and anti-cytotoxic t-lymphocyte-associated antigen 4 in a preclinical mouse model of urothelial carcinoma. Int J Urol 2019;26:414–22. doi: https://doi.org/10.1111/iju.13878.
[29] Min Joh H et al. Reactive oxygen species-related plasma effects on the apoptosis of human bladder cancer cells in atmospheric pressure pulsed plasma jets. Appl Phys Lett 2012;101. doi: https://doi.org/10.1063/1.4742742.
[30] Tavares-da-Silva, E., *et al.* Cold atmospheric plasma, a novel approach against bladder cancer, with higher sensitivity for the high-grade cell line. *Biology (Basel)* **2021**, *10*, 10.3390/biology10010041.
[31] Keidar M et al. Cold plasma selectivity and the possibility of a paradigm shift in cancer therapy. Br J Cancer 2011;105:1295–301. doi: https://doi.org/10.1038/bjc.2011.386.
[32] Metelmann H-R et al. Clinical experience with cold plasma in the treatment of locally advanced head and neck cancer. Clin Plas Med 2018;9:6–13. doi: https://doi.org/10.1016/j.cpme.2017.09.001.
[33] Akter, M., *et al.* Non-thermal atmospheric pressure bio-compatible plasma stimulates apoptosis via p38/mapk mechanism in u87 malignant glioblastoma. *Cancers (Basel)* **2020**, *12*, 10.3390/cancers12010245.
[34] Vaquero, J., *et al.* Cold-atmospheric plasma induces tumor cell death in preclinical in vivo and in vitro models of human cholangiocarcinoma. *Cancers (Basel)* **2020**, *12*, 10.3390/cancers12051280.
[35] Ahn HJ et al. Atmospheric-pressure plasma jet induces apoptosis involving mitochondria via generation of free radicals. PLoS ONE 2011;6:e28154.
[36] Ruwan Kumara MH et al. Non-thermal gas plasma-induced endoplasmic reticulum stress mediates apoptosis in human colon cancer cells. Oncol Rep 2016;36:2268–74. doi: https://doi.org/10.3892/or.2016.5038.
[37] Turrini E et al. Cold atmospheric plasma induces apoptosis and oxidative stress pathway regulation in t-lymphoblastoid leukemia cells. Oxid Med Cell Longev 2017;2017:4271065. doi: https://doi.org/10.1155/2017/4271065.
[38] Gandhirajan RK et al. Cytochrome c oxidase inhibition and cold plasma-derived oxidants synergize in melanoma cell death induction. Sci Rep 2018;8:12734. doi: https://doi.org/10.1038/s41598-018-31031-2.
[39] Galluzzi L et al. Molecular mechanisms of cell death: Recommendations of the nomenclature committee on cell death 2018. Cell Death Differ 2018;25:486–541. doi: https://doi.org/10.1038/s41418-017-0012-4.
[40] Xie Y et al. Fgf/fgfr signaling in health and disease. Signal Transduct Target Ther 2020;5:181. doi: https://doi.org/10.1038/s41392-020-00222-7.
[41] Roubal K et al. Erdafitinib: A novel therapy for fgfr-mutated urothelial cancer. Am J Health Syst Pharm 2020;77:346–51. doi: https://doi.org/10.1093/ajhp/zxz329.
[42] Ohiro Y et al. A novel p53-inducible apoptogenic gene, prg3, encodes a homologue of the apoptosis-inducing factor (aif). FEBS Lett 2002;524:163–71. doi: https://doi.org/10.1016/s0014-5793(02)03049-1.
[43] Marshall KR et al. The human apoptosis-inducing protein amid is an oxidoreductase with a modified flavin cofactor and DNA binding activity. J Biol Chem 2005;280:30735–40. doi: https://doi.org/10.1074/jbc.M414018200.
[44] Horikoshi N et al. Isolation of differentially expressed cdnas from p53-dependent apoptotic cells: Activation of the human homologue of the drosophila peroxidasin gene. Biochem Biophys Res Commun 1999;261:864–9. doi: https://doi.org/10.1006/bbrc.1999.1123.
[45] Gong M et al. DNA binding suppresses human aif-m2 activity and provides a connection between redox chemistry, reactive oxygen species, and apoptosis. J Biol Chem 2007;282:30331–40. doi: https://doi.org/10.1074/jbc.M703713200.
[46] Miriyala S et al. Novel role of 4-hydroxy-2-nonenal in aifm2-mediated mitochondrial stress signaling. Free Radic Biol Med 2016;91:68–80. doi: https://doi.org/10.1016/j.freeradbiomed.2015.12.002.
[47] Bilyy R et al. Amid: New insights on its intracellular localization and expression at apoptosis. Apoptosis 2008;13:729–32. doi: https://doi.org/10.1007/s10495-008-0198-5.
[48] Jablonowski H et al. Research on plasma medicine-relevant plasma–liquid interaction: What happened in the past five years? Clin Plas Med 2015;3:42–52. doi: https://doi.org/10.1016/j.cpme.2015.11.003.
[49] Freund E et al. Gas plasma-oxidized liquids for cancer treatment: Preclinical relevance, immuno-oncology, and clinical obstacles. IEEE Transactions on Radiation and Plasma Medical Sciences 2021;5:761–74. doi: https://doi.org/10.1109/trpms.2020.3029982.
[50] Smolkova, B., *et al.* Non-thermal plasma, as a new physicochemical source, to induce redox imbalance and subsequent cell death in liver cancer cell lines. *Cell Physiol Biochem* **2019**, *52*, 119-140, 10.33594/000000009.
[51] Freund E et al. Physical plasma-treated saline promotes an immunogenic phenotype in ct26 colon cancer cells in vitro and in vivo. Sci Rep 2019;9:634. doi: https://doi.org/10.1038/s41598-018-37169-3.
[52] Bauer G. The synergistic effect between hydrogen peroxide and nitrite, two long-lived molecular species from cold atmospheric plasma, triggers tumor cells to induce their own cell death. Redox Biol 2019;26:. doi: https://doi.org/10.1016/j.redox.2019.101291101291.
[53] Wardman P. Fluorescent and luminescent probes for measurement of oxidative and nitrosative species in cells and tissues: Progress, pitfalls, and prospects. Free Radic Biol Med 2007;43:995–1022. doi: https://doi.org/10.1016/j.freeradbiomed.2007.06.026.
[54] Lin A et al. Nanosecond-pulsed dbd plasma-generated reactive oxygen species trigger immunogenic cell death in a549 lung carcinoma cells through intracellular oxidative stress. Int J Mol Sci 2017;18:966. doi: https://doi.org/10.3390/ijms18050966.
[55] Wolff CM et al. Combination treatment with cold physical plasma and pulsed electric fields augments ros production and cytotoxicity in lymphoma. Cancers (Basel) 2020;12:845. doi: https://doi.org/10.3390/cancers12040845.
[56] Yusupov M et al. Synergistic effect of electric field and lipid oxidation on the permeability of cell membranes. Biochim Biophys Acta Gen Subj 2017;1861:839–47. doi: https://doi.org/10.1016/j.bbagen.2017.01.030.
[57] Van der Paal J et al. Effect of lipid peroxidation on membrane permeability of cancer and normal cells subjected to oxidative stress. Chem Sci 2016;7:489–98. doi: https://doi.org/10.1039/c5sc02311d.
[58] Yan D et al. Toward understanding the selective anticancer capacity of cold atmospheric plasma–a model based on aquaporins (review). Biointerphases 2015;10:. doi: https://doi.org/10.1116/1.4938020040801.
[59] Bekeschus S et al. Redox stimulation of human thp-1 monocytes in response to cold physical plasma. Oxid Med Cell Longev 2016;2016:5910695. doi: https://doi.org/10.1155/2016/5910695.
[60] Ahn HJ et al. Targeting cancer cells with reactive oxygen and nitrogen species generated by atmospheric-pressure air plasma. PLoS ONE 2014;9:e86173.
[61] Van Loenhout, J., *et al.* Auranofin and cold atmospheric plasma synergize to trigger distinct cell death mechanisms and immunogenic responses in glioblastoma. *Cells* **2021**, *10*, 10.3390/cells10112936.
[62] Lawrence A et al. Evidence for the role of a peroxidase compound i-type intermediate in the oxidation of glutathione, nadh, ascorbate, and dichlorofluorescin by cytochrome c/h2o2. Implications for oxidative stress during apoptosis. J Biol Chem 2003;278:29410–9. doi: https://doi.org/10.1074/jbc.M300054200.
[63] Burkitt MJ et al. Cytochrome c is a potent catalyst of dichlorofluorescin oxidation: Implications for the role of reactive oxygen species in apoptosis. Biochem Biophys Res Commun 2001;282:329–33. doi: https://doi.org/10.1006/bbrc.2001.4578.
[64] Ross DT et al. Systematic variation in gene expression patterns in human cancer cell lines. Nat Genet 2000;24:227–35. doi: https://doi.org/10.1038/73432.
[65] Boukamp P et al. Normal keratinization in a spontaneously immortalized aneuploid human keratinocyte cell line. J Cell Biol 1988;106:761–71.
[66] Moran MC et al. Characterization of human keratinocyte cell lines for barrier studies. JID Innov 2021;1:. doi: https://doi.org/10.1016/j.xjidi.2021.100018100018.
[67] Girard PM et al. Synergistic effect of h2o2 and no2 in cell death induced by cold atmospheric he plasma. Sci Rep 2016;6:29098. doi: https://doi.org/10.1038/srep29098.
[68] Biscop, E., *et al.* Influence of cell type and culture medium on determining cancer selectivity of cold atmospheric plasma treatment. *Cancers (Basel)* **2019**, *11*, 10.3390/cancers11091287.
[69] Bundscherer L et al. Viability of human blood leukocytes compared with their respective cell lines after plasma treatment. Plasma Med 2013;3:71–80. doi: https://doi.org/10.1615/PlasmaMed.2013008538.
[70] Bekeschus S et al. Tumor cell metabolism correlates with resistance to gas plasma treatment: The evaluation of three dogmas. Free Radic Biol Med 2021;167:12–28. doi: https://doi.org/10.1016/j.freeradbiomed.2021.02.035.

[71] Novo N et al. The apoptosis-inducing factor family: Moonlighting proteins in the crosstalk between mitochondria and nuclei. IUBMB Life 2021;73:568–81. doi: https://doi.org/10.1002/iub.2390.
[72] Murahashi H et al. Possible contribution of apoptosis-inducing factor (aif) and reactive oxygen species (ros) to uvb-induced caspase-independent cell death in the t cell line jurkat. J Leukoc Biol 2003;73:399–406. doi: https://doi.org/10.1189/jlb.0702335.
[73] Shelar SB et al. Thioredoxin-dependent regulation of aif-mediated DNA damage. Free Radic Biol Med 2015;87:125–36. doi: https://doi.org/10.1016/j.freeradbiomed.2015.06.029.
[74] Schmidt A et al. Redox-regulation of activator protein 1 family members in blood cancer cell lines exposed to cold physical plasma-treated medium. Plasma Process Polym 2016;13:1179–88. doi: https://doi.org/10.1002/ppap.201600090.
[75] Schmidt A et al. Nrf2 signaling and inflammation are key events in physical plasma-spurred wound healing. Theranostics 2019;9:1066–84. doi: https://doi.org/10.7150/thno.29754.
[76] Bersuker K et al. The coq oxidoreductase fsp1 acts parallel to gpx4 to inhibit ferroptosis. Nature 2019;575:688–92. doi: https://doi.org/10.1038/s41586-019-1705-2.
[77] Furuta R et al. Intracellular responses to reactive oxygen and nitrogen species, and lipid peroxidation in apoptotic cells cultivated in plasma-activated medium. Plasma Process Polym 2017;14:1700123. doi: https://doi.org/10.1002/ppap.201700123.
[78] Yadav DK et al. Insight into the molecular dynamic simulation studies of reactive oxygen species in native skin membrane. Front Pharmacol 2018;9:644. doi: https://doi.org/10.3389/fphar.2018.00644.
[79] Redelman-Sidi G et al. The mechanism of action of bcg therapy for bladder cancer–a current perspective. Nat Rev Urol 2014;11:153–62. doi: https://doi.org/10.1038/nrurol.2014.15.
[80] Lin A et al. Non-thermal plasma as a unique delivery system of short-lived reactive oxygen and nitrogen species for immunogenic cell death in melanoma cells. Adv Sci (Weinh) 2019;6:1802062. doi: https://doi.org/10.1002/advs.201802062.
[81] Clemen R et al. Gas plasma technology augments ovalbumin immunogenicity and ot-ii t cell activation conferring tumor protection in mice. Adv Sci (Weinh) 2021;8:2003395. doi: https://doi.org/10.1002/advs.202003395.
[82] Clemen R et al. Physical plasma-treated skin cancer cells amplify tumor cytotoxicity of human natural killer (nk) cells. Cancers (Basel) 2020;12:3575. doi: https://doi.org/10.3390/cancers12123575.
[83] Mahdikia H et al. Gas plasma irradiation of breast cancers promotes immunogenicity, tumor reduction, and an abscopal effect in vivo. Oncoimmunology 2021;10:1859731. doi: https://doi.org/10.1080/2162402X.2020.1859731.